OPEN ACCESS

Catalysis & Surface ARTICLE

Microfluidic synthesis enables highly dispersed Ru/$ZrPO_4$ catalyst for hydrodeoxygenation of lignin-derived phenolic compounds

Riyang Shu,[1] Guangming Liang,[1] Yuankai Lin,[1] Yu Chen,[1] Zhipeng Tian,[1] Chao Wang,[1] Jingtao Zhang,[1] Qiyu Liu,[3,*] and Ying Xu[2,*]

*Correspondence: liuqiyu@gdut.edu.cn (Q. L.); xuying@hqu.edu.cn (Y. X.)

Received: September 20, 2025; Accepted: November 8, 2025; Published Online: January 9, 2026; https://doi.org/10.59717/j.xinn-energy.2026.100130

GRAPHICAL ABSTRACT

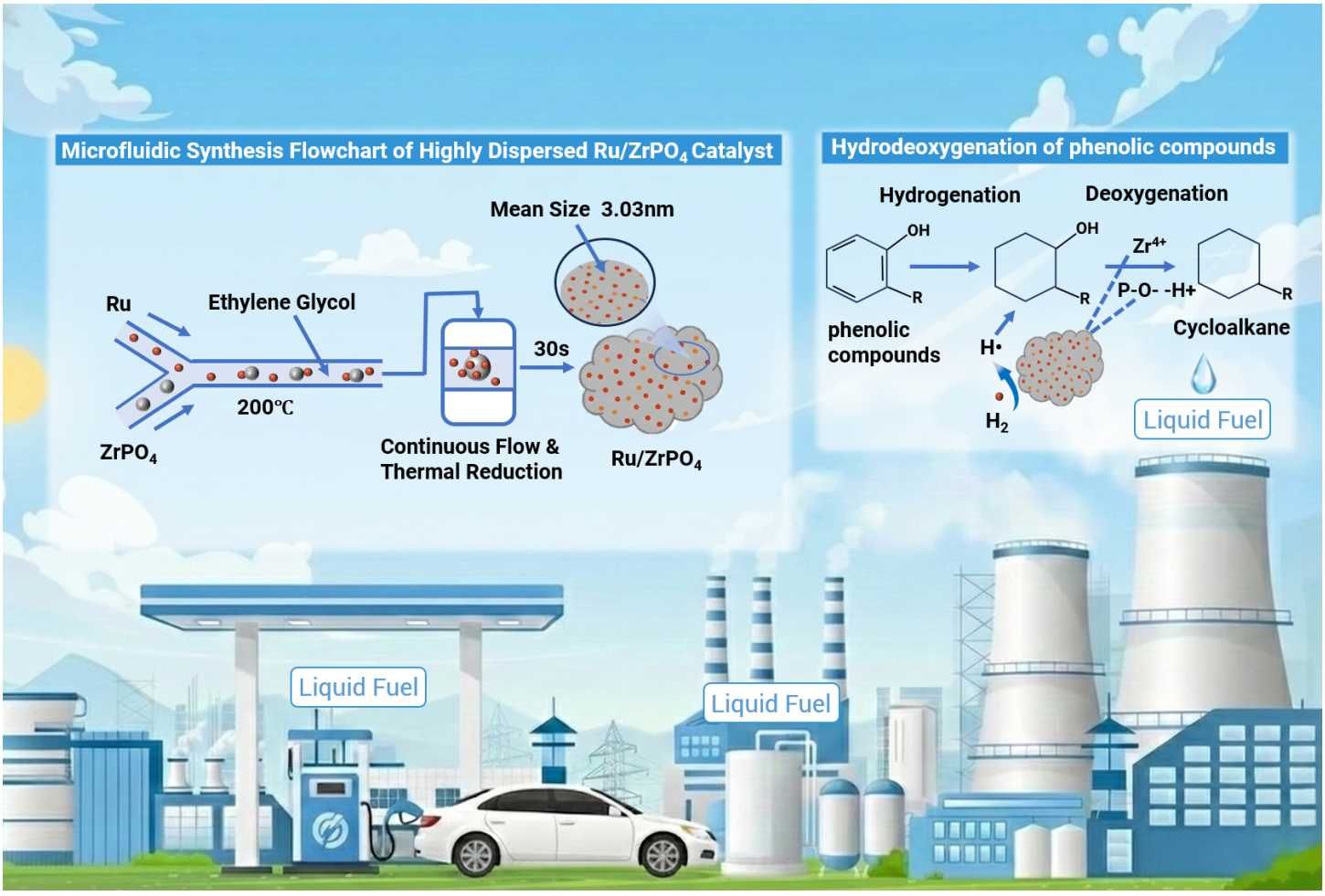

PUBLIC SUMMARY

- Highly dispersed Ru/$ZrPO_4$ catalyst synthesized via microfluidic-assisted ethylene glycol reduction.
- Ru/$ZrPO_4$-MIC shows small Ru particle size (3.03 nm) with excellent dispersion and H_2 activation.
- Complete guaiacol conversion with 97.9% cyclohexane selectivity under mild conditions.
- Superior activity and stability compared with impregnation and hydrothermal catalysts.
- Microfluidic strategy enables low metal loading and is applicable to other noble metal catalysts.

ARTICLE Catalysis & Surface

OPEN ACCESS

Microfluidic synthesis enables highly dispersed $Ru/ZrPO_4$ catalyst for hydrodeoxygenation of lignin-derived phenolic compounds

Riyang Shu,[1] Guangming Liang,[1] Yuankai Lin,[1] Yu Chen,[1] Zhipeng Tian,[1] Chao Wang,[1] Jingtao Zhang,[1] Qiyu Liu,[3,*] and Ying Xu[2,*]

[1]Guangdong Provincial Key Laboratory of Functional Soft Condensed Matter, School of Materials and Energy, Guangdong University of Technology, Guangzhou 510006, PR China

[2]Academy of Advanced Carbon Conversion Technology, Huaqiao University, Xiamen, Fujian Province 361021, China

[3]Guangdong Provincial Key Laboratory of Plant Resources Biorefinery, School of Chemical Engineering and Light Industry, Guangdong University of Technology, Guangzhou 510006, China

*Correspondence: liuqiyu@gdut.edu.cn (Q. L.); xuying@hqu.edu.cn (Y. X.)

Received: September 20, 2025; Accepted: November 8, 2025; Published Online: January 9, 2026; https://doi.org/10.59717/j.xinn-energy.2026.100130

Citation: Shu R., Liang G., Lin Y., et al. (2026). Microfluidic synthesis enables highly dispersed $Ru/ZrPO_4$ catalyst for hydrodeoxygenation of lignin-derived phenolic compounds. *The Innovation Energy* **3**:100130.

To address the demand for efficient hydrodeoxygenation (HDO) of lignin-derived phenolic compounds into high-value hydrocarbon fuels, this study designed and synthesized highly dispersed $Ru/ZrPO_4$ catalysts by employing a novel microfluidic technology coupled with ethylene glycol thermal reduction. The traditional impregnation ($Ru/ZrPO_4$-IMP) and the hydrothermal method ($Ru/ZrPO_4$-HYD) were also conducted to compare with the microfluidic method ($Ru/ZrPO_4$-MIC). Comprehensive characterizations via XRD, TEM, XPS, H_2-TPD and NH_3-TPD reveal that $Ru/ZrPO_4$-MIC presents superior properties of small average Ru particle size (3.03 nm), excellent metal dispersion, outstanding hydrogen dissociation capability and suitable acid strength, which improve the HDO performance significantly. Under mild reaction condition (240 °C, 1 MPa H_2), the $Ru/ZrPO_4$-MIC achieves complete conversion of guaiacol and 97.9% selectivity toward cyclohexane, significantly outperforming the $Ru/ZrPO_4$-IMP (47.4%) and $Ru/ZrPO_4$-HYD (79.7%) catalysts, as well as most of the reported catalysts. Comparative studies confirm that the microfluidic approach effectively prevents metal agglomeration and enhances metal dispersion. $Ru/ZrPO_4$-MIC catalyst also presents a high stability after 5 recycles, with little catalytic activity loss. Moreover, in the HDO upgrading of lignin oil, hydrocarbon content increases from 10.5% to 91.8%. This novel microfluidic method is also suitable for the preparation of other highly dispersed noble metal-based catalysts, which enables to achieve high catalytic activity under the low metal loading.

INTRODUCTION

Fossil fuels have played a key role in global industrialization. While, their limited resources and environmental pollution pose severe energy and environmental challenges.[1,2] Biomass energy, with its renewability and carbon-neutral characteristics, has become a critical direction for the alternative of fossil fuels.[3,4] Lignin is one of the three components of lignocellulosic biomass, as well as the only one aromatic polymer in nature. It suffers from the low energy density. This problem can be solved by pyrolysis to yield lignin oil that rich in phenolic compounds (e.g., guaiacol).[5-7] However, the lignin oil still can't match with the high calorific value and chemical stability of fossil fuels because of its abundance of oxygen atoms and unsaturated bonds.[8,9] Hydrodeoxygenation (HDO) technology enables to effectively reduce oxygen-containing groups and break unsaturated bonds (e.g., C=C, C=O), representing one of the most promising strategies to produce high-quality fuels.

The synergy between metal sites and acid sites is crucial for an efficient HDO catalyst.[10-12] Metal sites utilize the unique electronic structures to adsorb hydrogen molecules and dissociate H–H bonds, generating active hydrogen source for subsequent hydrogenation procedure. Simultaneously, acid sites on the carrier interact with C-O bonds in substrate, reducing activation energy of the bonds through electron cloud rearrangement to improve the breakage of C-O bonds. Metals are typically categorized into noble metals (*e.g.*, Pt, Ru, Pd) and non-noble metals. Non-noble metals (*e.g.*, Co, Ni, Mo) are cost-effective but require high reaction temperature to show catalytic activity.[13-15] Noble metal catalysts enables to present superior hydrogenation capability under mild condition.[16-19] For instance, our previous study prepared a Pt/Al_2O_3-TiO_2 catalyst with photochemical method and achieved 100% guaiacol conversion at 260 °C with cyclohexane selectivity of 99.9%.[20] Newman *et al.* synthesized different Ru-based catalysts on C, SiO_2, Al_2O_3, and TiO_2 supports, which were employed for the HDO of phenol at 300 °C. The high dispersed Ru-based catalyst presented a high phenol conversion.[21] Yan *et al.* compared the Ru/ZSM-5 and Ru/BEA catalysts with atomically dispersed Ru metal in the guaiacol HDO reaction. Ru/ZSM-5 achieved 67.7% yield of cyclohexane at the temperature of 250 °C.[22] Overall, the results show that metal particle size and metal dispersion significantly impact HDO efficiency. As for the acid sites, phosphate carriers such as $AlPO_4$ and $ZrPO_4$ provide both Brønsted and Lewis acid sites, which facilitates the deoxygenation procedure. Our previous study developed a $Ni/AlPO_4$ catalyst, demonstrating excellent catalytic activity and stability in the HDO of guaiacol. 99.9% conversion and 91.1% yield of cyclohexane were obtained at 250 °C.[23] Han *et al.* compared the catalytic performance of $Co/ZrPO_4$ and $Ni/ZrPO_4$ catalysts in the guaiacol HDO at 300 °C. Results showed that the acid site derived from $ZrPO_4$ support promoted the deoxygenation process significantly.[24]

Traditional catalyst preparation methods such as co-impregnation generally suffer from metal agglomeration during high-temperature reduction, leading to large metal particles that makes negative effect on the specific catalytic activity, against the green chemistry concept. To address this challenge, researchers have recently devoted efforts to developing various novel synthesis strategies capable of achieving high metal dispersion.[25-30] For instance, constructing single-atom catalysts is regarded as an effective approach to realizing high metal dispersion. Hu et al. successfully synthesized a Mo single-atom catalyst anchored on an LDH-derived support via cationic vacancy engineering, which exhibited nearly 100% cyclohexane yield and excellent stability in the HDO of guaiacol under mild conditions.[31] Additionally, other strategies, such as metal-organic framework (MOF) derived methods, have also shown remarkable progress in constructing highly dispersed nanocatalysts.[32] However, the above strategies often involve complex multi-step synthesis processes, which limits their general applicability and potential for scalable production to some extent. Microfluidic continuous synthesis enables to address this problem. The core advantages of the microfluidic approach lie in its ability to provide precise fluidic control and uniform reaction conditions, thereby overcoming limitations inherent in traditional batch synthesis such as reaction heterogeneity and particle agglomeration. Zhang *et al.* designed a rapid approach to synthesize Pt-Bi bimetallic nanoparticles in microfluidic tube, which realized the particle size controlling. By adjusting reaction temperature and solvent, Pt_1Bi_1 and Pt_1Bi_2 nanoparticles with tunable sizes were obtained, exhibiting superior methanol electrocatalytic activity.[33] Similarly, Kunal *et al.* used a continuous flow system with multistage microreactors to synthesize Rh and RhAg alloy nanoparticles, suppressing agglomeration and ripening via hydrodynamic confinement.[34] These successful cases further underscore the inherent benefits of microfluidic synthesis. By tuning preparation parameters, the distribution of metal particle size enables to be regulated and the particle growth can be controlled. However, the supported metal-based catalysts using microfluidic methods have not yet been reported before.

In this work, we employed microfluidic technology coupled with ethylene glycol reduction to prepare the high dispersed $Ru/ZrPO_4$ catalyst, which was systematically evaluated in the HDO of lignin-derived phenolic compounds and lignin oil. High dispersed $Ru/ZrPO_4$ catalyst enables to take full advantage of the catalytic activity of each metal atom that meets the demand of

green chemistry. Different preparation methods were compared to produce $Ru/ZrPO_4$ catalyst, including impregnation, hydrothermal reduction and microfluidic synthesis. The process parameters during microfluidic synthesis were also investigated and a series of catalyst characterizations were conducted. In addition, the preparation of other Ru-based catalysts using microfluidic synthesis was also tested to confirm the method universality. This novel microfluidic method offers a potential alternative for the development of fine catalyst designs.

MATERIALS AND METHODS

Materials

$RuCl_3$, $NH_4H_2PO_4$, $ZrOCl_2{\cdot}8H_2O$, ethanol, *n*-octane solvent, guaiacol, and other phenolic compounds were derived from Shanghai Aladdin Co., Ltd. All reagents were analytical grade. Lignin oil was obtained from the cotton straw pyrolysis and fractional condensation was used to extract the phenolic components based on the reported study.[35]

Catalyst preparation

Preparation of $ZrPO_4$ carrier: The preparation process of the $ZrPO_4$ carrier was conducted as following. Under stirring condition at room temperature, $NH_4H_2PO_4$ solution (1.0 mol/L, 100 mL) was added to $ZrOCl_2{\cdot}8H_2O$ solution (1.0 mol/L, 50mL). Then the mixture was placed in a high-pressure reactor at 120 °C all day long. The resulting white solution was centrifugally washed alternately with water and ethanol, and dried at 80 °C for 18 h to obtain the $ZrPO_4$ carrier.

Preparation of $Ru/ZrPO_4$-IMP catalyst: The $Ru/ZrPO_4$-IMP catalyst was prepared using impregnation method. 1 g of $ZrPO_4$ was added in a crucible with specific amount of $RuCl_3$ solution (4wt% Ru loading) and deionized water. After magnetic stirring at 300 r/min for 6 h, the mixture was dried at 60 °C. Then the crucible was transferred into a vacuum drying oven at 100 °C overnight. A tube furnace was used to conduct the reduction procedure at 400 °C with a hydrogen flow rate of 60 mL/min for 3 h. Finally, the supported $Ru/ZrPO_4$-IMP catalyst was obtained.

Preparation of $Ru/ZrPO_4$-HYD catalyst: The $Ru/ZrPO_4$-HYD catalyst was prepared by hydrothermal method with ethylene glycol reduction. Based on our previous study,[36] 1 g of $ZrPO_4$ was added in a hydrothermal autoclave. Then, a calculated specific volume of $RuCl_3$ solution (4wt% Ru loading) and 50 mL ethylene glycol solvent were added and heated to 200 °C under stirring at a speed of 300 r/min for 2 h. After cooling down, the catalyst sample was centrifuged and placed in a vacuum drying oven at 70 °C overnight for drying to obtain the $Ru/ZrPO_4$-HYD catalyst.

Preparation of $Ru/ZrPO_4$-MIC catalyst: The $Ru/ZrPO_4$-MIC catalyst was prepared by microfluidic method, combining with ethylene glycol reduction, as shown in Figure 1A. As the ethylene glycol reduction method mentioned above, the highly dispersed metal-based catalyst can be obtained by reacting the ethylene glycol solution of Ru precursor at 200 °C. Besides, the confinement effect of microfluidic method further facilitates the self-assembly and the high metal dispersion during the preparation process. The precursor solutions consist of 1 g of $ZrPO_4$ carrier mixed with 50 mL of ethylene glycol solution and specific volume of $RuCl_3$ solution (4wt% Ru loading). The microfluidic system setup consists of an injection pump, a T-junction, a capillary tube (inner diameter 1.5 mm, outer diameter 1.9 mm, length 2.0 m) coiled in an oil bath maintained at 200 °C, and a cooling section. First, the precursor solutions were separately sealed in syringes, and then injected into a fixed capillary at a controlled flow rate. The two solutions were mixed together through a T-junction. After the mixture passed through the heated microfluidic capillary in heating oil bath (200 °C), the reduction process was completed. Then, the microfluidic capillary was introduced into cooling parts and a collection tube. The total process took only 30 seconds. The collected $Ru/ZrPO_4$-MIC catalyst was centrifuged and washed, and then placed in a vacuum drying oven at 70 °C overnight.

Preparation of other Ru-based catalysts with microfluidic method: In order to test the universal applicability of the microfluidic method, other Ru-based catalysts with microfluidic method were also tested. The preparation procedures are as following. When preparing Ru/TiO_2, Ru/Al_2O_3, and Ru/ZrO_2 catalysts, TiO_2, Al_2O_3, and ZrO_2 supports were used. 1 g of each carrier was added with 50 mL of ethylene glycol to form one solution. The other solution was specific volume of $RuCl_3$ solution (4wt% Ru loading). Both of them were injected simultaneously in a flow rate of 1.5 mL/min to mix together. The afterward procedures were conducted as above. When preparing $Pt/ZrPO_4$, $Pd/ZrPO_4$ and $Ag/ZrPO_4$ catalysts, the procedures were the same, and specific volume of noble metal solution (4wt% noble metal loading) were used.

Catalyst characterization

The nitrogen adsorption-desorption isotherms at 77K were measured using a Micromeritics ASAP 2460 analyzer. The specific surface area was calculated based on the Brunauer-Emmett-Teller (BET) method. The average pore diameter was measured by the Barrett-Joyner-Halenda (BJH) method from the desorption branch. Inductively coupled plasma-atomic emission spectrometry (ICP-AES) was conducted on the instrument of OPTIMA 8000. X-ray powder diffraction (XRD) analysis was carried out using a Shimadzu XRD- 6000 instrument in the 2θ range of 5°-90°. The catalyst crystallite size was calculated based on the Debye-Scherrer equation:

$$D = \frac{K \times \lambda}{\beta \times cos\theta}$$

where D represents the crystallite size (Å). K=0.89. λ=1.5406 Å. θ is the diffraction angle, and β is the full width at half-maximum. Scanning electron microscopy (SEM) images were acquired using a Thermo Fisher Quattro S device. Additionally, transmission electron microscopy (TEM), high-resolution TEM (HRTEM), scanning TEM (STEM) images, and energy-dispersive spectroscopy (EDS) images were from Thermo Talos F200S instrument. Ammonia temperature-programmed desorption (NH_3-TPD) experiments were conducted on a Bayer BELCAT-A instrument equipped with a thermal conductivity detector (TCD) to study the catalyst acidity. X-ray photoelectron spectroscopy (XPS) measurements were performed using a Thermo Scientific ESCALAB 250Xi system, with the C 1s peak at 284.8eV used as the reference. Finally, electron paramagnetic resonance (EPR) data were collected using a Bruker EMX PLUS spectrometer. Thermogravimetric analysis (TGA) was conducted in the instrument of NETZSCH-STA 449 F5 for catalyst detection. H_2 programmed temperature desorption (H_2-TPD) was carried out on a chemisorption instrument equipped a TCD. The Ru metal dispersion is calculated based on the quantitative results of H_2-TPD and ICP-AES. The standard assumption for calculating dispersion based on H_2-TPD is that one H_2 molecule undergoes dissociative adsorption on two surface Ru atoms (H: Ru surface = 1:1). The formula is as follows:

$$D(\%) = \frac{2 \times Hads \times M_{Ru}}{m \times \omega} \times 100\%$$

where H_{ads} is the hydrogen adsorption amount, M_{Ru} = 101.07 g/mol, m is the sample mass, and ω is the Ru metal loading.

HDO of phenolic compounds and lignin oil

The HDO reaction of phenolic compounds was carried out in a 50 mL high-pressure 316L stainless steel reactor (Four-station parallel reactor, Guizhou Shanli Experimental Instrument Co., Ltd). The specific experimental procedure is as following. First, 0.1 g of the phenolic compound was dissolved in 20 mL of *n*-octane, with addition of 0.05 g of the catalyst. Then purge the reactor with hydrogen to 1 MPa (displacing air three times at first), and heat the reactor to the preset temperature at a rate of 3 °C/min while stirred at 400 rpm. The reaction time was maintained for 4 hours.

For the HDO upgrading treatment of lignin oil, 3.0 g of raw lignin bio-oil was added to 20 mL of *n*-octane to extract the components of phenolic compounds. Then, the HDO reaction of the lignin oil was conducted following the same steps as the HDO of phenolic compounds. After reaction, the reactor was cooled down. Filtration were used to collect the liquid products and their chemical composition was analyzed using a gas chromatography-mass spectrometry (GC-MS, Thermo Fisher Scientific Trace 1300) equipped with a TG-5 Sil MS capillary column (30m×0.25mm×0.25μm film thickness). Substrate conversion and product selectivity were calculated by Equation (1) and Equation (2).

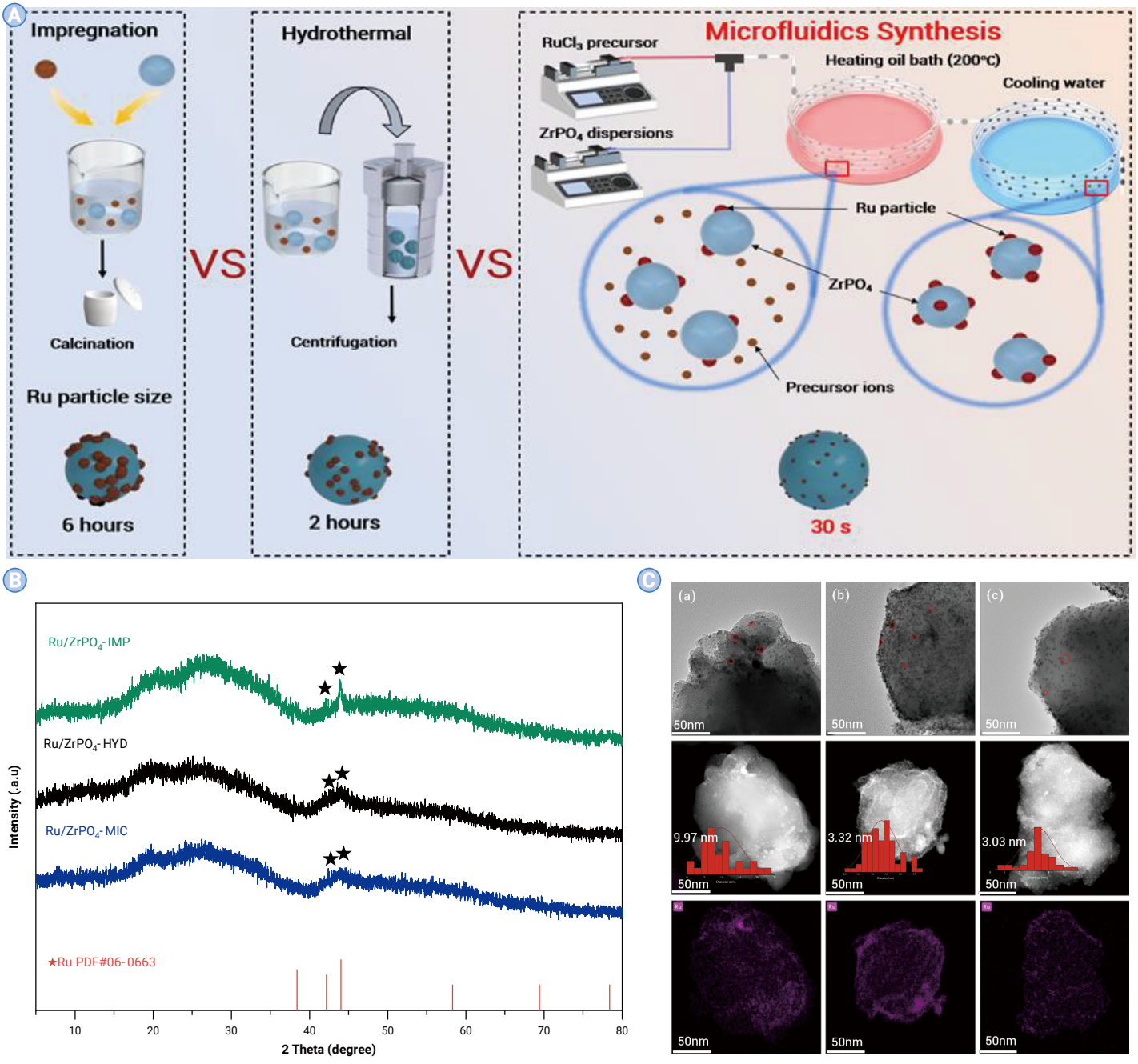

Figure 1. (A) Schematic diagram of the microfluidic synthesis procedure of Ru/$ZrPO_4$-MIC catalyst compared with traditional impregnation and hydrothermal methods. (B) XRD patterns of the different Ru/$ZrPO_4$ catalysts. (C) TEM images and EDS energy spectra of (a) Ru/$ZrPO_4$-IMP, (b) Ru/$ZrPO_4$-HYD, and (c) Ru/$ZrPO_4$-MIC catalysts.

$$Conversion\,(\%) = 100\% \times \frac{Moles_{initial\ GUA} - Moles_{remaining\ GUA}}{Moles_{initial\ GUA}} \quad (1)$$

$$Selectivity\,(\%) = 100\% \times \frac{Moles_{product_i}}{\sum Moles_{product}} \quad (2)$$

RESULTS AND DISCUSSION

Catalyst characterization

Various characterizations were conducted to investigate the differences in the physicochemical properties among Ru/$ZrPO_4$ catalysts. The XRD patterns in Figure 1B show that the characteristic diffraction peaks of Ru phase are at 42.1° (002) and 44.0° (101), which matches the standard Ru pattern of PDF#06-0663. This indicates that the Ru particle in the catalyst is in the metallic phase rather than oxide phase. The Ru metal peak in the Ru/$ZrPO_4$-IMP catalyst is sharp, and the Ru particle size is approximately 9.67 nm. For the other two catalysts, the positions of Ru characteristic peaks are broad peaks. The average grain sizes of Ru on Ru/$ZrPO_4$-HYD and Ru/$ZrPO_4$-MIC are 3.95 nm and 3.15 nm, respectively. Ru/$ZrPO_4$-MIC catalyst shows the best Ru dispersion, which is probably related to the confinement effect of microfluidic method. With a limited capillary volume, the contact between the support and the Ru precursor solution is restricted. As the ethylene glycol reduction reaction proceeds, highly dispersed Ru is loaded onto the $ZrPO_4$ support surface.

TEM measurement was employed to further observe and analyze the distribution and morphology of Ru metal particles in the catalysts, as images presented in Figure 1C. The sizes of 50 randomly selected Ru nanoparticles within the region are statistically analyzed. The Ru particle sizes of Ru/$ZrPO_4$-IMP, Ru/$ZrPO_4$-HYD and Ru/$ZrPO_4$-MIC are 9.97 nm, 3.32 nm and 3.03 nm, respectively. The results derived from TEM are consistent with those deduced from the XRD analysis. The Ru/$ZrPO_4$-MIC catalyst exhibits excellent loading

Table 1. Surface property and Ru metal property of different $Ru/ZrPO_4$ catalysts.

Catalysts	Specific surface area[a] (m^2/g)	Total porosity[b] (nm)	Ru content[c] (wt.%)	Ru dispersion[d] (%)
$Ru/ZrPO_4$-IMP	62.93	6.14	3.91	8.89
$Ru/ZrPO_4$-HYD	70.83	7.52	3.11	32.58
$Ru/ZrPO_4$-MIC	76.11	6.57	2.85	35.09

[a] Data measured by BET method. [b] Data measured by BJH method. [c] Data measured by ICP-AES. [d] Based on the H_2-TPD quantitative measurement.

and uniform Ru dispersion, with no agglomeration observed. During the occurrence of the Ru precursor reduction in the microfluidic capillary, Ru particle agglomeration on the loading surface can be suppressed significantly. Ethylene glycol not only acts as a reducing agent but also serves as a protective agent to remain the metallic phase of Ru and prevent from the agglomeration of Ru nanoparticles. As seen from the images, all Ru particles are loaded onto the support, indicating that the nucleation process of Ru preferentially occurs heterogeneously on the surface. In addition, the dispersion state of Ru particles is further verified by EDS scanning, and the results are consistent with the statistical analysis.

The specific surface area and metal loading of the catalysts are measured, as the results presented in Table 1. Among them, the $Ru/ZrPO_4$-IMP catalyst has a specific surface area of 62.93 m^2/g and a pore diameter of 6.14 nm. The $Ru/ZrPO_4$-HYD catalyst exhibits a specific surface area of 70.83 m^2/g and a pore diameter of 7.52 nm. In contrast, the $Ru/ZrPO_4$-MIC catalyst presents a specific surface area of 76.11 m^2/g and a pore diameter of 6.57 nm. This may be related to the pore-blocking effect after metal loading.[37] The $Ru/ZrPO_4$-IMP catalyst prepared by the impregnation method has relatively large particles, which tends to cover the mesopores on the surface of the support. In comparison, the $Ru/ZrPO_4$-MIC catalyst prepared by the microfluidic technology has much smaller particles, which is beneficial for the subsequent hydrogenation process. According to the metal-loading results, the Ru loadings of $Ru/ZrPO_4$-IMP, $Ru/ZrPO_4$-HYD, and $Ru/ZrPO_4$-MIC are 3.91%, 3.11%, and 2.85%, respectively. The significant deviation from the expected proportion may be attributed to the relatively small surface area of the support.[38] However, considering the preparation time of the three catalysts, the loading result of $Ru/ZrPO_4$-MIC can be reasonable. Moreover, based on the quantitative results of H_2-TPD and ICP-AES, the Ru metal dispersion is also provided. Results show that $Ru/ZrPO_4$-MIC possesses the highest Ru dispersion, with the value of 35.09%, which is superior to $Ru/ZrPO_4$-IMP (8.89%) and $Ru/ZrPO_4$-HYD (32.58%).

XPS technology was utilized to observe the electronic states of different Ru 3d orbitals. The Ru electronic states of the catalysts prepared by the three methods are similar. According to relevant literature,[21] the Ru 3d peak at 284.8 eV overlaps with the calibrated carbon peak. The characteristic peak corresponding to Ru^0 $3d_{3/2}$ is at 284.8 eV, and the characteristic peak corresponding to Ru^0 $3d_{5/2}$ is near 280.5 eV. The Ru^{2+} $3d_{5/2}$ peak corresponds to a value near 281.7 eV, corresponding to RuOx. Regarding the carbon peak C 1s, the XPS spectra all exhibit double peaks. Specifically, the peaks near 284.8 eV and 286 eV correspond to the C-C and C-OH chemical bonds, respectively. The peak of Ru^0 $3d_{5/2}$ at 280.4 eV is higher than the standard peak at 280.2 eV. This may be due to the electron exchange between Ru and the highly electronegative P on the support, resulting in an increase of binding energy.[37] By deconvoluting the spectra to calculate the Ru^0/Ru^{2+} ratio, the ratios for $Ru/ZrPO_4$-IMP, $Ru/ZrPO_4$-HYD and $Ru/ZrPO_4$-MIC are 1.59, 1.95, and 1.99, respectively. The proportion of Ru^0 of the $Ru/ZrPO_4$-MIC catalyst is the highest, which demonstrates that the microfluidic method successfully reduces and loads Ru metal onto the surface of $ZrPO_4$ in a short time. Combining with TEM image results, $Ru/ZrPO_4$-MIC possesses the special features of smallest particle size and highest Ru^0/Ru^{2+} ratio at the same time. As for the reason, based on the aforementioned analysis of the positive binding energy shift of Ru $3d_{5/2}$ and the increased Ru^0/Ru^{2+}ratio, the synergistic phenomenon demonstrates the formation of a strong metal-support electronic interaction in the $Ru/ZrPO_4$-MIC catalyst. The interaction strength is likely influenced by the preparation method, as evidenced by that microfluidic technology provides the rapid mixing and stable mass transfer conditions and promotes the uniform distribution of metal precursors on the support surface.[39] Meanwhile, the fast reduction kinetics of the ethylene glycol reductant within the confined space facilitate the formation of Ru nanoparticles with uniform size and strong adhesion to the support. This strong electronic interaction may modulate the catalytic activity and selectivity in HDO reactions by influencing the adsorption property of substrate.

The hydrogen adsorption and dissociation abilities of different $Ru/ZrPO_4$ catalysts were compared through the H_2-TPD experiment. The adsorption peaks are classified into a low-temperature peak (100-300 °C), a medium-temperature peak (300-500 °C), and a high-temperature peak (above 500 °C).[39] The low-temperature adsorption peak corresponds to physically adsorbed hydrogen on the surface or weakly adsorbed hydrogen. The medium-temperature adsorption peak corresponds to metallic hydrogen, that is, dissociated hydrogen at the metal sites. The high-temperature adsorption peak corresponds to hydrogen with a strong interaction with the support or the hydrogen spillover phenomenon. The $Ru/ZrPO_4$-IMP catalyst has a medium-temperature adsorption peak at 372.2 °C, with a relatively low peak intensity. This is mainly caused by the agglomeration of Ru particles. Agglomeration leads to a decrease in the dissociation of hydrogen on the available metal surface, which also corresponds to the smallest adsorption peak area. Both $Ru/ZrPO_4$-HYD and $Ru/ZrPO_4$-MIC have an adsorption peak at the metal sites in the medium- temperature peak region. The adsorption peak temperature of $Ru/ZrPO_4$-MIC is 394.5 °C, which is a higher adsorption temperature peak, indicating better dispersion of Ru and a stronger interaction with the support. Based on the peak areas, the quantitative hydrogen adsorption amount is also calculated out, and the results show that the hydrogen adsorption amount of $Ru/ZrPO_4$-MIC is the largest.

NH_3-TPD measurement was used to characterize the acidity property of the different $Ru/ZrPO_4$ catalysts, including the acid amount (reflected by the total amount of desorbed NH_3) and the acid strength (indicated by the desorption peak temperature). Based on the desorption temperature range, acid sites are typically classified as weak acid (<200 °C), medium acid (200-400 °C), and strong acid (>400 °C)[36] (Figure 2C). The $Ru/ZrPO_4$ catalysts prepared by different synthesis methods exhibit significant differences. As shown in Table S1, $Ru/ZrPO_4$-IMP has the lowest total acid amount of 0.73 mmol/g, with desorption peaks at 108.2 °C, 390.5 °C, and 565.0 °C, indicating the coexistence of weak, medium, and strong acid sites on its surface. In contrast, the total acid amount of $Ru/ZrPO_4$-MIC increases to 2.16 mmol/g, with desorption peaks at 159.6 °C and 385.9 °C, demonstrating that its predominant acid sites are weak and medium acids. It is notable that the peak of medium acid is very large, and the medium acid is the suitable acid species for HDO reaction. Weak acid can't cleave the C-O bond efficiently and strong acid probably leads to the condensation of intermediate products. $Ru/ZrPO_4$-HYD possesses the highest total acid amount of 3.56 mmol/g. Its desorption peaks are observed at 148.6 °C, 379.2 °C, and 492.8 °C, indicating that this catalyst also features a distribution of acid sites ranging from weak acid to strong acid. Overall, although $Ru/ZrPO_4$-MIC catalyst hasn't presented the highest total acid amount, the dominant of medium acid makes it possess the superiority on the HDO reaction.

Catalytic HDO of guaiacol

Regarding the role of ethylene glycol during catalyst preparation, TGA characterization was conducted to detect the decomposition products in the $Ru/ZrPO_4$-MIC catalyst. The TG curve in Figure S1 shows no characteristic weight loss peak of ethylene glycol within the volatilization temperature range (195–200 °C). The mass change observed before 200 °C is primarily attributed to the removal of crystalline and adsorbed water. This result indicates that ethylene glycol has been effectively removed during the catalyst

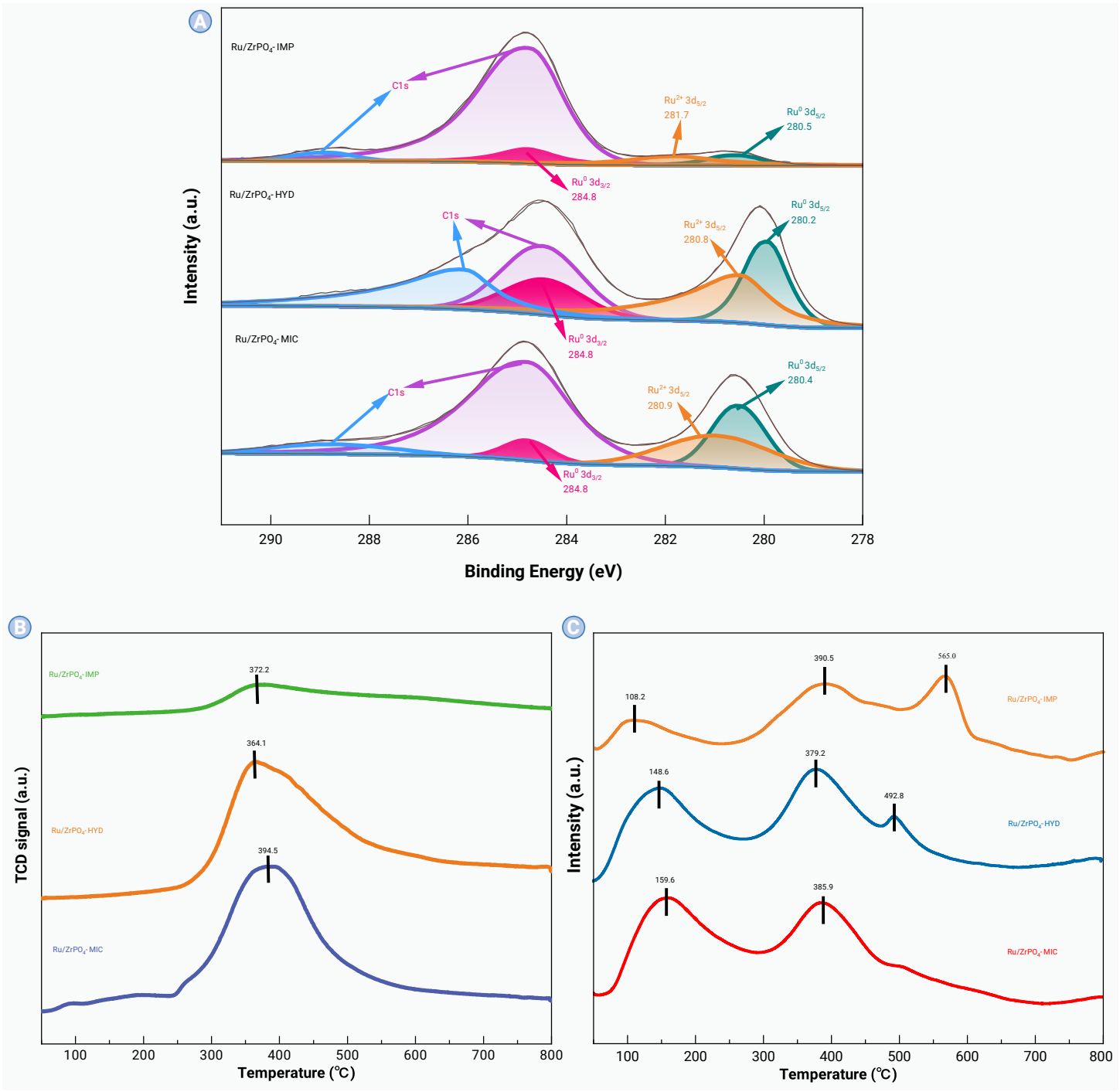

Figure 2. (A) XPS profiles in the C 1s and Ru 3d regions of the different $Ru/ZrPO_4$ catalysts. (B) H_2-TPD spectra of different $Ru/ZrPO_4$ catalysts. (C) NH_3-TPD profiles of the $Ru/ZrPO_4$ catalysts prepared by different methods.

washing process and the effect of ethylene glycol residues on the catalytic performance has been eliminated. Table 2 presents the reaction results of guaiacol reacting for 4 hours on different $Ru/ZrPO_4$ catalysts at 240 °C and 1.0 MPa H_2. The conversion rates of guaiacol all reach over 99%, achieving complete conversion. The main reaction products are cyclohexane, cyclohexanol, methoxycyclohexanol, and phenol. The deoxygenation efficiency of $Ru/ZrPO_4$-IMP is relatively low, with a cyclohexane yield of only 47.4%. As for the $Ru/ZrPO_4$-HYD catalyst, the selectivity increases from 47.4% to 79.7%. And the $Ru/ZrPO_4$-MIC catalyst presents the highest cyclohexane selectivity of 97.9%. When a blank experiment is conducted on the single $ZrPO_4$, the conversion rate is only 9.5%, indicating that the loading of metallic Ru is a key factor affecting conversion and selectivity. The occurrence of HDO reactions needs active hydrogen generated by the dissociation of active metals. And catalysts with smaller metal particle size and higher metal dispersion expose more active metal sites, facilitating the occurrence of HDO. During the ethylene glycol reduction process, ethylene glycol acts as both a reducing agent and an inhibitor of metal agglomeration, resulting in a higher dispersion of Ru compared to the impregnation method. In terms of reaction activity, highly dispersed Ru sites can expose more adsorbed and dissociated hydrogen, thus enhancing the breakage of C(Ar)-OCH_3 and C(Ar)-OH bonds, and improving deoxygenation activity. Comparing the $Ru/ZrPO_4$-HYD and $Ru/ZrPO_4$-MIC catalysts, the difference in their activities is not significant. This can be primarily attributed to the fact that both reduction methods employ ethylene glycol as the reducing agent and share the same reduction mechanism. However, the practical advantage of the microfluidic method mainly lies in the synthesis process itself. Compared to the hydrothermal

Table 2. HDO performance of guaiacol over different $Ru/ZrPO_4$ catalysts.

Catalysts	Conversion (%)	Product selectivity (%)			
			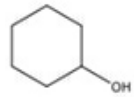	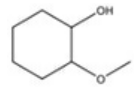	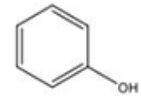
$Ru/ZrPO_4$–IMP	99.2	47.4	39.7	12.9	–
$Ru/ZrPO_4$–HYD	99.6	79.7	12.2	1.5	6.4
$Ru/ZrPO_4$–MIC	99.9	97.9	2.1	–	–
$ZrPO_4$	9.5	–	–	–	–

Condition: 20 mL *n*–octane solvent, 0.1 g guaiacol, 0.05 g catalyst, 240 °C, 1 MPa H_2, 4 h.

batch process ($Ru/ZrPO_4$-HYD) that takes several hours, microfluidic synthesis ($Ru/ZrPO_4$-MIC) is a continuous process that reduces the reaction time to only 30 seconds. This continuous and rapid synthesis approach avoids batch-to-batch variations and ensures good reproducibility. Moreover, the microfluidic method possesses the feature of confinement effect, which enables to achieve strong metal-support interaction and improve the HDO efficiency and catalyst stability.

The optimal reaction conditions were investigated in detail by employing the $Ru/ZrPO_4$-MIC catalyst. Reaction condition parameters such as hydrogen pressure, reaction temperature, and reaction time can significantly influence the reaction efficiency. As seen from Figure 3A, increasing the hydrogen pressure improves the conversion rate and alkane selectivity. When the hydrogen pressure is 0.6 MPa, the guaiacol conversion and the alkanes yield reach 71.3% and 25.4%, respectively. Additionally, the higher the hydrogen pressure achieves the deeper HDO degree to form cyclohexane. When hydrogen pressure is 1 MPa, the guaiacol conversion and the cyclohexane yield both exceed 95%. However, when the hydrogen pressure exceeds 1.2 MPa, there are no significant changes in the conversion rate and product selectivity. Under the condition of low hydrogen pressures, only a low-concentration phenol intermediate is detected, indicating that the catalyst has high hydrogenation activity and the substrate can be hydrogenated efficiently. In addition, the reaction temperature effect was also tested. Increasing the reaction temperature is beneficial to the conversion of guaiacol, as shown in Figure 3B. Guaiacol is completely converted at 210 °C with a reaction time of 4 h. Meanwhile, the cyclohexane yield increases with the enhancement of the reaction temperature. In contrast, the amount of the intermediate methoxycyclohexanol decreases as the reaction temperature rises. This is mainly because at low temperatures below 200 °C, the highly dispersed Ru metal surface first adsorbs the benzene ring plane to carry out the hydrogenation reaction, generating intermediate products cyclohexanol and methoxycyclohexanol. Moreover, the yield of intermediate cyclohexanol first increases and then decreases, indicating that methoxycyclohexanol is the primary product of the hydrogenation reaction, rather than cyclohexanol formed by demethoxylation.

The reaction time was also optimized to enhance the HDO of guaiacol. As seen from Figure 3C, the guaiacol conversion is 40.3% and the yield of alkanes is 26.6% after 1 h. After 3 h, the conversion rate exceeds 99% and the alkane selectivity reaches 72.6%. With the reaction time further extended to 4 h, the yield of cycloalkanes reaches 97.9%, achieving complete conversion and selectivity. Based on the above results, it can be reasonably deduced that the guaiacol molecule is first adsorbed onto the catalyst surface, where the C=C bonds in the aromatic ring and the C=O bond undergo hydrogenation at the Ru active sites, forming intermediates (such as 2-methoxycyclohexanol). This intermediate then undergoes cleavage of the C–O bond to yield cyclohexanol, which is finally dehydrated or directly deoxygenated to form the end product of cyclohexane. Moreover, the catalyst preparation process was also optimized and the effect of the injection flow rate was investigated. As results shown in Figure 3D, when the flow rate increases from 1 mL/min to 3 mL/min during catalyst preparation, the reaction conversion rate of catalyst first remains unchanged and then gradually decreases. The increase in flow rate corresponds to a shortening of the reaction time in the microfluidic capillary. The shortened reduction time means an increased difficulty in reducing metallic Ru, and the Ru^{3+} in the precursor is initially reduced to Ru^{2+} instead of Ru^0. When the flow rate is decreased, metal agglomeration may occur, along with potential capillary blockage. When the reaction flow rate is 2 mL/min, the reaction conversion rate of the catalyst drops to 72.8%. When the flow rate increases to 3mL/min, the reaction conversion rate of the catalyst further decreases to 50.6%. This may be due to the poor crystallinity of Ru produced by the reduction reaction, resulting in an inefficient reduction of Ru and affecting the conversion process of the reaction.[40] Therefore, 1.5 mL/min is adopted as the optimal injection parameter to prepare the $Ru/ZrPO_4$-MIC catalyst.

The $Ru/ZrPO_4$-MIC catalyst was used to conduct recycle in the HDO reactions of guaiacol to verify its stability (Figure S2). As the number of recycles increase, the guaiacol conversion remains basically unchanged while the cycloalkane selectivity decreases slightly. The cycloalkane selectivity decreases from 97.9% in the first reaction to 86.5% in the fifth reaction. To elucidate the reasons for the activity slight decline of the spent $Ru/ZrPO_4$-MIC catalyst after five recycles, a series of catalyst characterizations were conducted, including SEM, XRD and XPS measurements. SEM images in Figure S3 exhibit little morphology change, indicating the high stability of the catalyst. XRD patterns (Figure S4a) show that after five recycle reaction, the Ru characteristic peaks appear obviously, demonstrating grain growth and agglomeration of Ru nanoparticles. In addition, XPS analysis in Figure S4b indicates that the binding energy of the characteristic peak of Ru^0 $3d_{5/2}$ of the spent catalyst presents an increasing shift. This may be due to that the Ru metal particles are tend to be oxidized during long-term reaction.[41-43] The intensity increase of the two peaks of carbon phase (sp^2-carbon and sp^3-carbon) indicates the formation of carbon deposits.[44] In summary, the slight decline in catalytic activity is attributed to a combination of multiple factors, including the agglomeration of Ru metal particles, oxidation of active Ru sites, and carbon deposits on the catalyst surface. Moreover, we further extended the recycle number to evaluate the catalyst durability. Result in Figure S2 shows that after ten recycle, the guaiacol conversion decreases to approximately 50%, as well as the cyclohexane selectivity.

The comparison of this work with other similar reported studies is conducted and the results are shown in Table 3. In contrast to the reported Pt-based, Pd-based and Ru-based catalysts,[45-54] the HDO performance of $Ru/ZrPO_4$-MIC catalyst in this work is much outstanding. The superior HDO performance is due to that $Ru/ZrPO_4$-MIC catalyst possesses a high Ru metal dispersion derived from the confinement effect of microfluidic technology, which allows a full HDO effect at relative low temperatures under relative low hydrogen pressures. The quick preparation process is also the advantage of this novel method.

HDO of other phenolic compounds and lignin oil

The $Ru/ZrPO_4$-MIC catalyst was also employed for the HDO reactions of other lignin-derived phenolic compounds at 240 °C, including 4-methylguaiacol, anisole, eugenol, 2,6-dimethoxyphenol, phenol and diphenyl ether. The reaction results are presented in Table 4. For phenol and anisole those have simple structures with only one functional group, complete conversion can be achieved and the yield of the target alkane products can exceed 95%. For

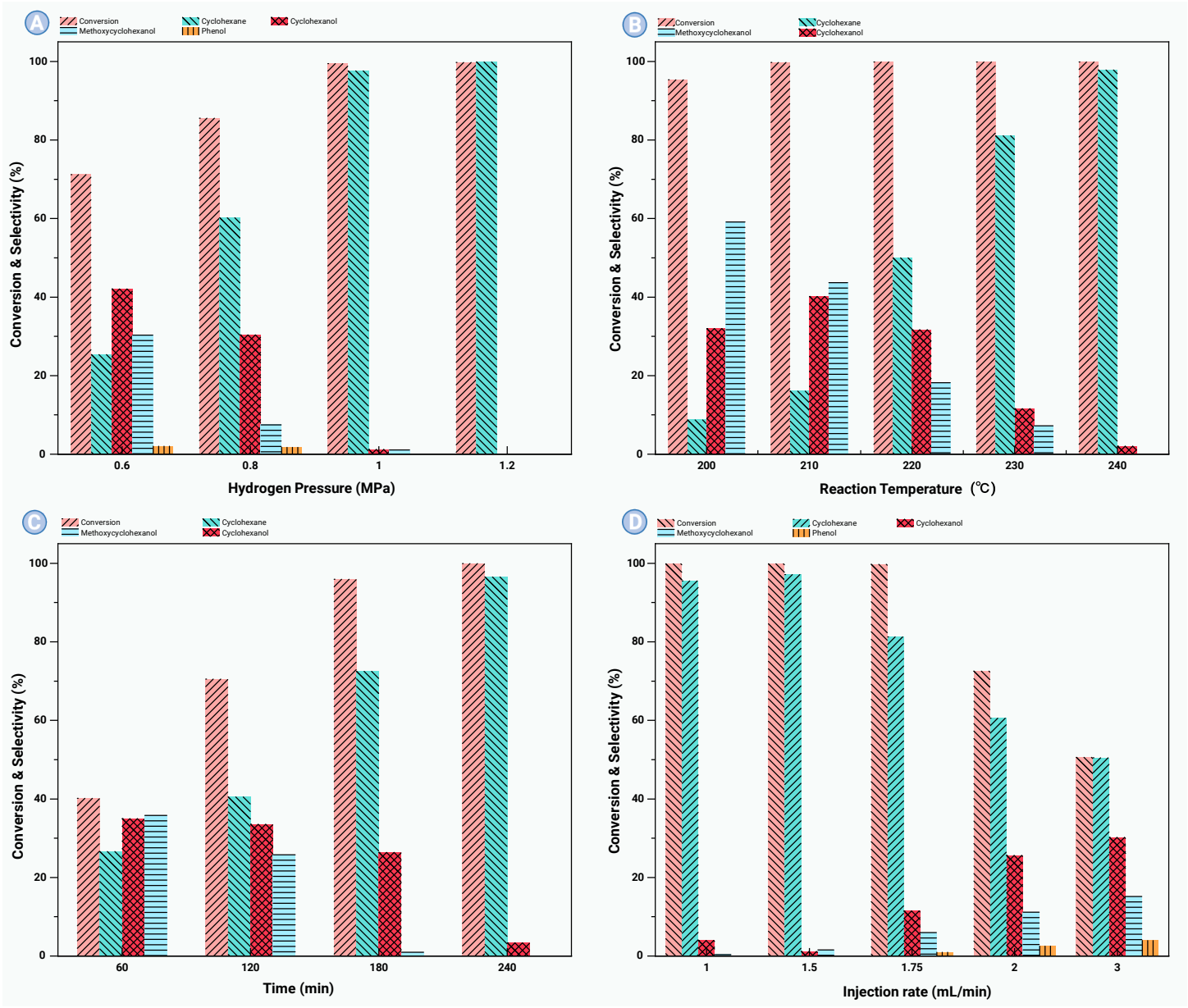

Figure 3. Effects of (A) hydrogen pressure (B) reaction temperature (C) reaction time (D) injection flow rate on the HDO of guaiacol.

Table 3. Overview of guaiacol HDO catalysts based on the preparation condition and reaction performance.

Entry	Catalyst	Catalyst preparation temperature (°C)	Catalyst preparation time	Reaction temperature (°C)	Reaction hydrogen pressure (MPa)	Cyclohexane yield (%)	Reference
1	Pt/Zeolite HY(5.1)	350	3 h	240	3	69	[45]
2	Pt/ZSM-5/Al_2O_3	420	3 h	300	4	67	[46]
3	Pt/TiO_2	500	4 h	280	1	95	[47]
4	Pt-Mo/TiO_2	260	3 h	285	4	69	[48]
5	TiO_2-Pd/SiO_2	450	2 h	280	2	80	[49]
6	Ru/BEA-12.5	550	6 h	250	4	72	[50]
7	Ru/Cl(5)/TiO_2	250	2 h	240	1	70	[51]
8	Ru/TiO_2	ultraviolet radiation	4 h	260	1	91	[52]
9	Ru-Co/C	600	3 h	260	1	77	[53]
10	Ni/SiO_2 + Hβ(50)	600	2 h	140	3	91.7	[54]
11	Ru/$ZrPO_4$-MIC	200	30 s	240	1	98	This work

Table 4. HDO results of other typical phenolic compounds on Ru/$ZrPO_4$-MIC catalyst.

Substrates	Conversion (%)	Product selectivity (%)
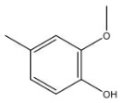	99.9	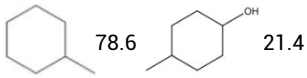 78.6 21.4
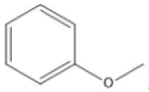	99.9	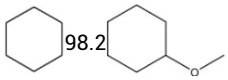 98.2 1.8
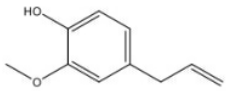	99.9	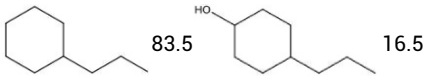 83.5 16.5
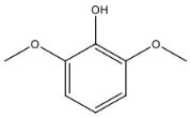	99.9	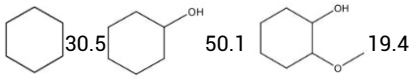 30.5 50.1 19.4
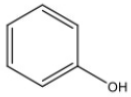	99.9	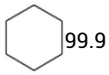 99.9
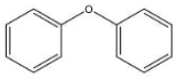	99.9	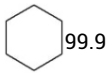 99.9

Condition: 20 mL *n*-octane, 0.1 g phenolic compounds, 0.05 g catalyst, 1 MPa H_2, 4 h, 240 °C.

more complex monomers with two or more functional groups, the selectivity of the target alkane decreases after the reaction, indicating that the presence of functional groups affects the reaction activity and thus influences the distribution of reaction products. The propyl group in eugenol affects the adsorption steric hindrance of the catalyst to the reaction substrate during the reaction, suppressing the occurrence of the HDO reaction. When 4-methylguaiacol undergoes the HDO reaction, the selectivity of methylcyclohexanol after the reaction is as high as 21.4%. This is mainly because the para-methyl group affects the electron density of the aromatic ring, resulting in a decrease in the removal rate of the Caryl- OR (R=H or CH_3) bond. 2,6-Dimethoxyphenol exhibits high selectivity towards oxygen-containing cyclic alcohols (e.g., methoxycyclohexanol), which may be attributed to the strong electron-donating effects of the two methoxy groups. This electron enrichment increases the electron density on the aromatic ring, thereby enhancing the strength of the C-O bond and posing certain challenges for the deoxygenation.[55,56] Consequently, the reaction pathway tends to favor hydrogenation of the aromatic ring prior to C-O bond cleavage, leading to the observed formation of intermediate products. The dimer diphenyl ether shows higher reaction activity in the HDO reaction, which is mainly related to the relatively low bond energy of the dimer-connecting bond (210-310 KJ/mol).[55] Overall, the Ru/$ZrPO_4$-MIC catalyst efficiently removes the C-O bonds of lignin-derived phenols and accomplishes the conversion of phenolic compounds into alkane compounds, exhibiting high HDO reaction activity.

The Ru/$ZrPO_4$-MIC catalyst was also applied to the HDO upgrading process of lignin oil. The results of the component changes in the reaction over time are shown in Figure S5. The hydrocarbon content of the lignin oil increases from 10.5% to 91.8%. Most of the products are fully HDO products, including cycloalkanes (86.5%) and a small amount of straight-chain hydrocarbon products (5.3%). The proportions of alkylphenols and guaiacols after the reaction decrease to 2.3% and 0%, respectively. The detailed components of the lignin oil before and after the HDO upgrading are also listed in Table S2. During the reaction, the proportion of other oxygen-containing compounds is first increased and then decreased, mainly because phenolic compounds are first hydrogenated to form alcohol compounds. Overall, the Ru/$ZrPO_4$-MIC catalyst exhibits high HDO reaction activity on the complicated feedstock.

Extended application of microfluidic preparation methods

To verify the universality of this novel microfluidic preparation method, a series of different noble metal-based HDO catalysts were prepared and their catalytic activities for guaiacol HDO were tested. The results are shown in Figure 4. When Ru metal is loaded onto different supports (TiO_2, Al_2O_3, ZrO_2), the reaction conversion rates all reach over 95%, indicating that this method remains applicable for other different supports to achieve a high dispersion of Ru metal. Similarly, when different metals (Pt, Pd, Ag) are loaded onto the $ZrPO_4$ support, the reaction conversion rates can still reach over 95% as well, and the cyclohexane yields are above 70%. This also demonstrates that different noble metals all enables to be highly dispersed onto $ZrPO_4$ support through this novel microfluidic method in the same way. Overall, microfluidic technology coupled with ethylene glycol reduction can stabilize the metal particles to achieve a high dispersion, finally obtaining a high HDO catalytic activity. Based on a review of the literature and experimental results,[57,58] it is speculated that during the ethylene glycol reduction process, oxalic acid, which stabilizes the metal precursor, is first formed. Under the protective effect of oxalic acid, the metal colloid can be stably deposited onto the support surface, and then a reduction reaction occurs under the help of *in-situ* action heat. Therefore, there is no need to provide a high temperature for the metal reduction process, and a low temperature of only 200 °C is enough in this work.

CONCLUSIONS

In this study, an innovative approach combining microfluidic technology with the ethylene glycol reduction was employed to efficiently synthesize the Ru/$ZrPO_4$-MIC catalyst in one step, with Ru metal highly dispersed on the $ZrPO_4$ surface. This catalyst is compared with those prepared by the impregnation method and the hydrothermal method in terms of catalyst physicochemical property and catalytic activity. Characterization results show that the microfluidic prepared Ru/$ZrPO_4$-MIC catalyst exhibits an average Ru metal particle size of only 3.03 nm, with high metal dispersion and no obvious agglomeration. XPS and H_2-TPD analysis confirms the efficient metal reduction and the outstanding hydrogen activation capability. Ru/$ZrPO_4$-MIC catalyst achieves 99% conversion and 97.6% cyclohexane selectivity in the guaiacol HDO reaction at 240 °C, significantly outperforming Ru/$ZrPO_4$-IMP and Ru/$ZrPO_4$-HYD catalysts, as well as most of the reported studies. For the HDO of lignin oil, the hydrocarbon content increases from 10.5% to 91.8% (cycloalkanes accounting for 86.5%), meanwhile the proportions of alkylphenols and guaiacols decrease to 2.3% and 0%, respectively. Recycle tests indi-

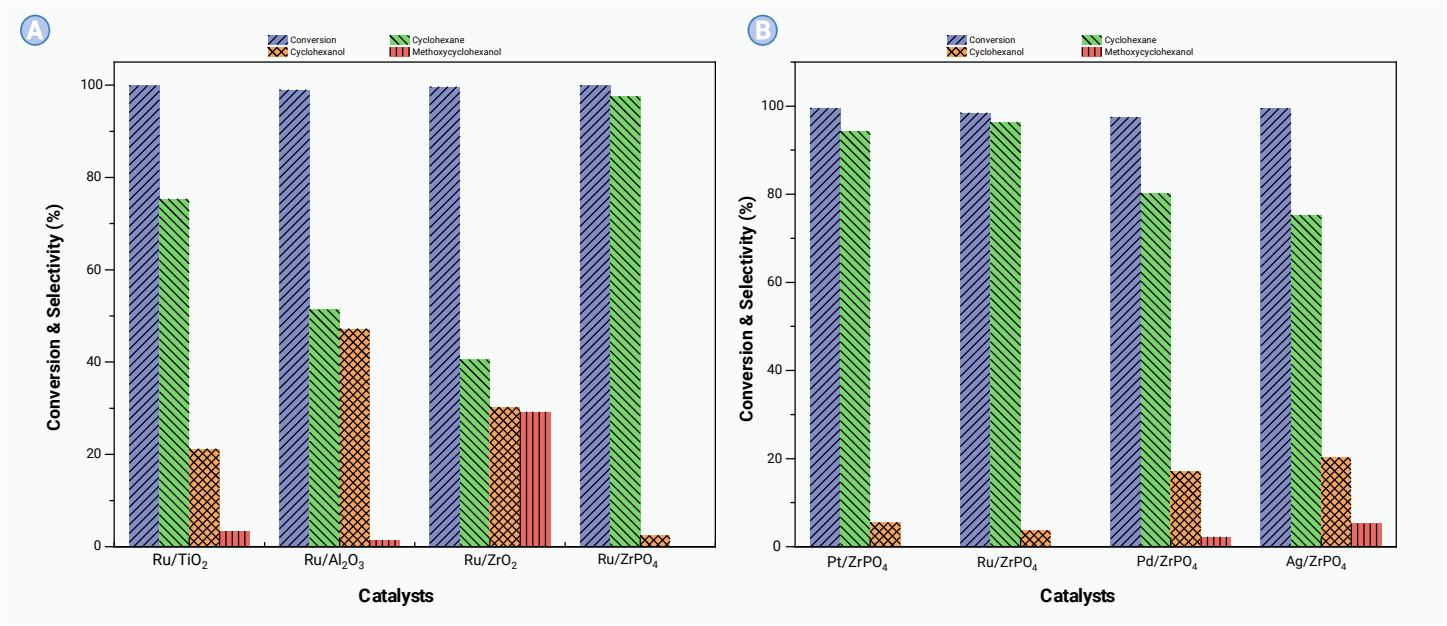

Figure 4. Effects of (A) different supports (B) different metal-based catalysts on the HDO of guaiacol.

cate that the conversion rate remains stable after 5 reaction recycles, with a slight decrease of cyclohexane selectivity (from 97.6% to 86.5%). Leveraging the advantages of confinement effect of microfluidic technology, the $Ru/ZrPO_4$-MIC catalyst excels in metal dispersion, catalytic activity, and stability. More importantly, this novel microfluidic preparation method presents a great universality, and the prepared different metal-based catalysts (including Ru/TiO_2, Ru/Al_2O_3, Ru/ZrO_2, $Pt/ZrPO_4$, $Pd/ZrPO_4$, $Ag/ZrPO_4$) are all showed high metal dispersion and high catalytic activity. This work provides a highly efficient catalyst system for the HDO of lignin-derived compounds towards green chemistry and holds significant value for biomass energy conversion. Furthermore, this method demonstrates promising prospects for industrial application, because its continuous-flow characteristics facilitate scalable production while maintaining consistent product quality. Additionally, its applicability to various metal and support systems indicates its potential as a versatile platform for catalyst preparation.

REFERENCES

1. Corma A., Iborra S., Velty A. (2007). Chemical routes for the transformation of biomass into chemicals. *Chem. Rev.* **107**:2411–2502. DOI:10.1021/cr050989d
2. Wong S.S., Shu R., Zhang J., Liu H., Yan N. (2020). Downstream processing of lignin derived feedstock into end products. *Chem. Soc. Rev.* **49**:5510–5560. DOI:10.1039/D0CS00278F
3. Wang J., Fu J., Zhao Z., et al. (2023). Benefit analysis of multi-approach biomass energy utilization toward carbon neutrality. *The Innovation* **4**:100423. DOI:10.1016/j.xinn.2023.100423
4. Xie X.Y., Li L.F., Wang X.Y., et al. (2025). Fractionation of high-yield noncondensed lignin and glucan oligomers from lignocellulose in a novel biphasic system. *J. Agric. Food Chem.* **73**:2880–2889. DOI:10.1021/acs.jafc.4c08261
5. Diao X.Y. and Ji N. (2023). Rational design of MoS_2-based catalysts toward lignin hydrodeoxygenation: Interplay of structure, catalysis, and stability. *J. Energy Chem.* **77**:601–631. DOI:10.1016/j.jechem.2022.12.017
6. Fang Z., Wen C., Zhang X., et al. (2025). Advance, challenge, and outlook of carbon-increasing strategies for producing sustainable high-energy-density jet fuels from lignocellulosic derivatives. *Innov. Energy* **2**:100093. DOI:10.59717/j.xinn-energy.2025.100093
7. Jiang S., Shu R., Wang A., et al. (2024). Efficient hydrodeoxygenation of lignin-derived phenolic compounds under acid-free conditions over carbon-supported NiMo catalysts. *Green Chem.* **26**:9330–9345. DOI:10.1039/D4GC02111A
8. Lahijani P., Mohammadi M., Mohamed A.R., et al. (2022). Upgrading biomass-derived pyrolysis bio-oil to bio-jet fuel through catalytic cracking and hydrodeoxygenation: A review of recent progress. *Energy Convers. Manage.* **268**:115956. DOI:10.1016/j.enconman.2022.115956
9. Cui Y. and Xu Y. (2024). Sustainable aviation fuel: Biomass fostered future aviation. *Innov. Energy* **1**:100007. DOI:10.59717/j.xinn-energy.2024.100007
10. Lv W., Jiang Y.Y., Tian K.H., et al. (2025). Constructing Ni–MgO wrapped by carbon sphere to prepare a defect-rich catalyst for the conversion of lignin-derived oligomers into hydrocarbons under mild conditions. *Chem. Eng. J.* **509**:161057. DOI:10.1016/j.cej.2024.161057
11. Shi D., Fang W., Zhang A., et al. (2025). Selective hydrodeoxygenation of furfural to 2-methylfuran over $Ni–Co/SiO_2$ bimetallic catalysts: Synergistic effect of metal and acid sites. *J. Environ. Chem. Eng.* **13**:116252. DOI:10.1016/j.jece.2025.116252
12. Wang X., Zhang Z., Yan Z., et al. (2023). Catalysts with metal–acid dual sites for selective hydrodeoxygenation of lignin derivatives: Progress in regulation strategies and applications. *Appl. Catal. A Gen.* **662**:119266. DOI:10.1016/j.apcata.2023.119266
13. Zhang X., Wu J.F., Li T., et al. (2022). Selective hydrodeoxygenation of lignin-derived phenolics to cycloalkanes over highly stable $NiAl_2O_4$ spinel-supported bifunctional catalysts. *Chem. Eng. J.* **429**:132181. DOI:10.1016/j.cej.2021.132181
14. Zhu Y., Ma Y., Sun Y., et al. (2024). Synchronous inverse valence modulation of Ni^{3+}/Co^{2+} over metal/metal-oxide heterojunction catalyst to promote hydrodeoxygenation performance of lignin derivatives. *J. Environ. Chem. Eng.* **12**:114758. DOI:10.1016/j.jece.2024.114758
15. Diao X.Y., Hao L.E., Shi Y.W., et al. (2025). Boosted hydrodeoxygenation of lignin and its derivatives to cycloalkanes over Ni catalysts with surface decoration of $AlPO_4$ species. *J. Energy Chem.* **104**:360–371. DOI:10.1016/j.jechem.2024.12.019
16. Chen Q., Tang D., Zhang Q., et al. (2025). Electron–metal support interactions enhanced by W–O–Zr interface in Pd–UiO-66 catalyst for efficient HDO of lignin derivatives at room temperature. *Chem. Eng. J.* **516**:163903. DOI:10.1016/j.cej.2025.163903
17. Wang H.L., Ruan H., Feng M.Q., et al. (2017). One-pot process for hydrodeoxygenation of lignin to alkanes using Ru-based bimetallic and bifunctional catalysts supported on zeolite Y. *ChemSusChem* **10**:1846–1856. DOI:10.1002/cssc.201700137
18. Kim H., Lee J., Kim Y., et al. (2024). Continuous flow upgrading of lignin pyrolysis oils to drop-in bio-hydrocarbon fuels over noble metal catalysts. *Chem. Eng. J.* **481**:148328. DOI:10.1016/j.cej.2023.148328
19. Chen L., Wang C., Shang N., et al. (2025). Highly dispersed Cu supported on urchin-like TiO_2 for efficient hydrodeoxygenation of lignin derivatives. *J. Catal.* **448**:116216. DOI:10.1016/j.jcat.2025.116216
20. Lin C., Deng Y., Lin Y., et al. (2025). Hydrodeoxygenation of lignin-derived phenolic compounds over highly dispersed $Pt/Al_2O_3–TiO_2$ composite catalyst. *Ind. Eng. Chem. Res.* **64**:8170–8178. DOI:10.1021/acs.iecr.5c00481
21. Newman C., Zhou X.B., Goundie B., et al. (2014). Effects of support identity and metal dispersion in supported ruthenium hydrodeoxygenation catalysts. *Appl. Catal. A Gen.* **477**:64–74. DOI:10.1016/j.apcata.2014.03.012
22. Yan P., Mensah J., Drewery M., et al. (2021). Role of metal support during Ru-catalysed hydrodeoxygenation of biocrude oil. *Appl. Catal. B Environ.* **281**:119470. DOI:10.1016/j.apcatb.2020.119470
23. Lin Y., Shu R., Yin T., et al. (2024). Catalytic hydrodeoxygenation of lignin-derived phenolic compounds with Ni-based aluminum phosphate catalyst. *Mol. Catal.* **567**:114444. DOI:10.1016/j.mcat.2023.114444
24. Han G.H., Lee M.W., Park S., et al. (2019). Revealing the factors determining the selectivity of guaiacol HDO reaction pathways using ZrP-supported Co and Ni catalysts. *J. Catal.* **377**:343–357. DOI:10.1016/j.jcat.2019.08.018
25. Khani Y., Kumar A., Hwang J., et al. (2025). Utilizing waste PET plastics derived metal–organic framework catalyst for the hydrodeoxygenation of lignin phenols. *Chem. Eng. J.* **517**:164392. DOI:10.1016/j.cej.2025.164392

26. Yin T., Ye Y.C., Jiang H., et al. (2025). Efficient hydrodeoxygenation of lignin-derived phenolic compounds over Ru-based catalyst with biochar and Al_2O_3 as composite support. *ChemSusChem* **18**:e202401870. DOI:10.1002/cssc.202401870
27. Lu X., Li Z.W., Zhao L., et al. (2025). Production of ethanol from cellulose in aqueous phase with Pt–Ni@C catalysts. *J. Fuel Chem. Technol.* **53**:863–871. DOI:10.1016/S1872-5813(25)60073-2
28. Qiu S.B., Xu Y., Weng Y.J., et al. (2016). Efficient hydrogenolysis of guaiacol over highly dispersed Ni/MCM-41 catalyst combined with HZSM-5. *Catalysts* **6**:134. DOI:10.3390/catal6090134
29. Ali H., Vandevyvere T., Lauwaert J., et al. (2023). Enhancing the anisole hydrodeoxygenation activity over Ni/Nb_2O_{5-x} by tuning the oxophilicity of the support. *Catal. Sci. Technol.* **13**:1140–1153. DOI:10.1039/D2CY01966A
30. Chen Y., Yang Y., Liu X., Jing F.M. (2024). O_2–H_2O_2 high-efficient co-oxidation of carbohydrate biomass to formic acid via Co_3O_4/C nanocatalyst. *Carb. Neutrality* **3**:23. DOI:10.1007/s43979-024-00023-7
31. Hu H.C., Ma D.C., Yi M., et al. (2025). Unveiling the enhancement of catalytic activity and stability by single-atom Mo anchored to cationic vacancy for catalytic hydrodeoxygenation of lignin to naphthenes. *Chem. Eng. J.* **505**:159303. DOI:10.1016/j.cej.2024.159303
32. Wu X., Li H., Ge F., et al. (2024). N-doped MOF–lignin hybrid catalyst for highly selective hydrodeoxygenation of lignin-derived phenols. *Chem. Eng. J.* **495**:153009. DOI:10.1016/j.cej.2024.153009
33. Zhang D., Wu F., Peng M., et al. (2015). One-step, facile and ultrafast synthesis of phase- and size-controlled Pt–Bi intermetallic nanocatalysts through continuous-flow microfluidics. *J. Am. Chem. Soc.* **137**:6263–6269. DOI:10.1021/jacs.5b03027
34. Kunal P., Roberts E.J., Riche C.T., et al. (2017). Continuous flow synthesis of Rh and RhAg alloy nanoparticle catalysts enables scalable production and improved morphological control. *Chem. Mater.* **29**:4341–4350. DOI:10.1021/acs.chemmater.7b00830
35. Ma S., Zhang L., Zhu L., Zhu X. (2018). Preparation of multipurpose bio-oil from rice husk by pyrolysis and fractional condensation. *J. Anal. Appl. Pyrolysis* **131**:113–119. DOI:10.1016/j.jaap.2018.01.017
36. Shu R.Y., Li R.X., Lin B.Q., et al. (2020). High dispersed Ru/SiO_2–ZrO_2 catalyst prepared by polyol reduction method and its catalytic applications in hydrodeoxygenation of phenolic compounds and pyrolysis lignin-oil. *Fuel* **265**:116962. DOI:10.1016/j.fuel.2019.116962
37. Lee S., Kim C.U., Kim J.C., et al. (2022). Enhanced catalytic activity of phosphorus-modified SSZ-13 zeolite in ethylene-to-propylene reaction by controlling acidity and intracrystalline diffusivity. *Chem. Eng. J.* **446**:137169. DOI:10.1016/j.cej.2022.137169
38. Nan L., Zhang H., Weitz D.A., et al. (2024). Development and future of droplet microfluidics. *Lab Chip* **24**:528–539. DOI:10.1039/D3LC00833A
39. Zhong Z., Luo B., Lin C., et al. (2023). Ultrafast microfluidic preparation of highly dispersed Ru/TiO_2 catalyst for hydrodeoxygenation of lignin-derived phenolic compounds. *Fuel* **340**:127567. DOI:10.1016/j.fuel.2022.127567
40. Gong F., Cai H., Zhou B., et al. (2018). Synthesis and characterization of $AlPO_4$ hollow microspheres and sorption properties for heavy metal ions. *Colloids Surf. A* **554**:286–295. DOI:10.1016/j.colsurfa.2018.06.034
41. Yan P., Mensah J., Drewery M., et al. (2021). Role of metal support during Ru-catalysed hydrodeoxygenation of biocrude oil. *Appl. Catal. B Environ.* **281**:119470. DOI:10.1016/j.apcatb.2020.119470
42. Deo S. and Janik M.J. (2021). Predicting an optimal oxide/metal catalytic interface for hydrodeoxygenation chemistry of biomass derivatives. *Catal. Sci. Technol.* **11**:5606–5618. DOI:10.1039/D1CY00938E
43. Zou J., Liang G., Yuwono J.A., et al. (2024). Size-dependent effects of Ru nanoparticles on Li–CO_2 batteries. *ACS Energy Lett.* **9**:5145–5155. DOI:10.1021/acsenergylett.4c01867
44. Yang Q., Qian H., Guo Y., et al. (2023). Rapid release of halocarbons from saline water by iron-based photochemistry. *Environ. Sci. Technol.* **57**:20781–20791. DOI:10.1021/acs.est.3c05112
45. Prabhudesai V.S., Yerrayya A., Gurrala L., Castaño P., Vinu R. (2024). Hydrodeoxygenation of mixtures of biomass-derived model compound oxygenates over Pt/HY catalysts. *Chem. Eng. Sci.* **288**:119800. DOI:10.1016/j.ces.2024.119800
46. Ju C., Li M., Fang Y., Tan T. (2018). Efficient hydro-deoxygenation of lignin-derived phenolic compounds over bifunctional catalysts with optimized acid/metal interactions. *Green Chem.* **20**:4492–4499. DOI:10.1039/C8GC02227A
47. Shu R., Lin B., Wang C., et al. (2019). Upgrading phenolic compounds and bio-oil through hydrodeoxygenation using highly dispersed Pt/TiO_2 catalyst. *Fuel* **239**:1083–1090. DOI:10.1016/j.fuel.2018.11.107
48. He Z., Hu M., Wang X. (2018). Highly effective hydrodeoxygenation of guaiacol on Pt/TiO_2: Promoter effects. *Catal. Today* **302**:136–145. DOI:10.1016/j.cattod.2017.06.036
49. Lu M., Zhu J., Li M., et al. (2016). TiO_2-modified Pd/SiO_2 for catalytic hydrodeoxygenation of guaiacol. *Energy Fuels* **30**:6671–6676. DOI:10.1021/acs.energyfuels.6b01267
50. Yan P., Mensah J., Drewery M., et al. (2021). Role of metal support during Ru-catalysed hydrodeoxygenation of biocrude oil. *Appl. Catal. B Environ.* **281**:119470. DOI:10.1016/j.apcatb.2020.119470
51. Wang X., Wu P., Wang Z., et al. (2021). Chlorine-modified Ru/TiO_2 catalyst for selective guaiacol hydrodeoxygenation. *ACS Sustainable Chem. Eng.* **9**:3083–3094. DOI:10.1021/acssuschemeng.0c08334
52. Shu R., Lin B., Zhang J., et al. (2019). Efficient catalytic hydrodeoxygenation of phenolic compounds and bio-oil over highly dispersed Ru/TiO_2. *Fuel Process. Technol.* **184**:12–18. DOI:10.1016/j.fuproc.2018.11.015
53. Xu Q., Shi Y., Yang L., Fan G., Li F. (2020). The promotional effect of surface Ru decoration on the catalytic performance of Co-based nanocatalysts for guaiacol hydrodeoxygenation. *Mol. Catal.* **497**:111224. DOI:10.1016/j.mcat.2020.111224
54. Wang X., Zhu S., Wang S., et al. (2019). Low-temperature hydrodeoxygenation of guaiacol into cyclohexane over Ni/SiO_2 catalyst combined with Hβ zeolite. *RSC Adv.* **9**:3868–3876. DOI:10.1039/C8RA09874J
55. Shu R.Y., Zhong Z.J., You H.Y., et al. (2021). Hydrodeoxygenation of lignin-derived phenolic compounds over Ru/TiO_2–CeO_2 catalyst prepared by photochemical reduction method. *J. Energy Inst.* **99**:1–8. DOI:10.1016/j.joei.2021.02.003
56. Viljava T.R., Saari E.R.M., Krause A.O.I. (2001). Simultaneous hydrodesulfurization and hydrodeoxygenation: Interactions between mercapto and methoxy groups. *Appl. Catal. A Gen.* **209**:33–43. DOI:10.1016/S0926-860X(00)00768-8
57. Joseyphus R.J., Matsumoto T., Takahashi H., et al. (2007). Designed synthesis of cobalt and its alloys by polyol process. *J. Solid State Chem.* **180**:3008–3018. DOI:10.1016/j.jssc.2007.07.035
58. Matsumoto T., Urakawa K., Joseyphus R.J., et al. (2007). Evaluation of polyol reduction for wet synthesis of metal nanoparticles. *Electrochemistry* **75**:969–975. DOI:10.5796/electrochemistry.75.969

FUNDING AND ACKNOWLEDGMENTS

The authors gratefully acknowledge the financial support of National Natural Science Foundation of China (No. 52576197, 52576207 and 22378077), Guangdong Basic and Applied Basic Research Foundation (No. 2024A1515011219), Fujian Provincial Natural Science Foundation of China (No. 2025J010038) and Guangzhou Science and Technology Plan Project (No. 2025D04J0008). We would like to thank Analysis and Test Center of Guangdong University of Technology for the TEM analysis.

AUTHOR CONTRIBUTIONS

All authors contributed to the manuscript and approved the final version.

DECLARATION OF INTERESTS

The authors declare no competing interests.

DATA AND CODE AVAILABILITY

Data are available from the corresponding author upon reasonable request.

SUPPLEMENTAL INFORMATION

It can be found online at: https://doi.org/10.59717/j.xinn-energy.2026.100130